JGR Atmospheres

RESEARCH ARTICLE
10.1029/2022JD037302

The Cycle of Large-Scale Aggregation in Tropical Radiative-Convective Equilibrium

Brittany D. Dygert[1] **and Dennis L. Hartmann**[1]

[1]Department of Atmospheric Sciences, University of Washington, Seattle, WA, USA

Key Points:

- Atmospheric transport from the warm region responds to the skewness of the surface temperature distribution
- Circulation influences low cloud amount through its effect on humidity above the boundary layer
- The interannual oscillation is strongest for sea surface temperatures roughly like the current tropics

Supporting Information:

Supporting Information may be found in the online version of this article.

Correspondence to:

B. D. Dygert,
bdygert@uw.edu

Citation:

Dygert, B. D., & Hartmann, D. L. (2023). The cycle of large-scale aggregation in tropical radiative-convective equilibrium. *Journal of Geophysical Research: Atmospheres*, *128*, e2022JD037302. https://doi.org/10.1029/2022JD037302

Received 21 JUN 2022
Accepted 24 MAR 2023

Abstract In numerical experiments in tropical radiative-convective equilibrium with interactive sea surface temperature (SST), the interaction between SST gradients and circulation can lead to an inter-annual oscillation between aggregated and relatively disaggregated convection. We investigate these oscillations in a global aquaplanet model with uniform insolation, no rotation, and slab ocean. The large-scale circulation organizes into warm convective regions and cooler subsiding regions. The cycle is characterized by variations in the surface temperature contrast between these warm and cold regions and the fraction of the domain that is subsiding. The temperature contrast grows as the warm region warms, the cool region cools, and the subsiding region expands. When the temperature contrast has reached its maximum, the large-scale circulation becomes much more effective at removing energy from the warm region, which enables evaporative cooling and cloud shortwave reflection to rapidly cool the warm region. The efficiency of atmospheric transport in cooling the warm region is associated with positive skewness of the SST distribution and a minimum in the area of rising motion. During the decline of SST contrast, evaporative cooling declines in the subsiding region and the cold pool begins to warm. Low clouds in the subsiding region decline due to a decrease in longwave cooling above the boundary layer associated with decreased subsidence drying as the subsiding region expands. At temperatures warmer than the current tropics, the response of the hydrologic cycle to SST contrast becomes stronger, so that the oscillation speeds up, weakens in amplitude, and vanishes at sufficiently high temperatures.

Plain Language Summary In a simplified global climate model with no rotation, no land, and uniform solar heating, the world cycles between two extremes in which the sea surface temperature (SST) is more uniform and one in which strong contrasts develop between warm and cool regions. When the surface temperature contrast is large, interactions between convection, clouds, and circulation act to reduce the temperature contrast and return the state of the system to one with smaller temperature contrasts. The response of the atmospheric circulation to the shape of the surface temperature distribution is critical in suppressing the temperature contrast and triggering the oscillation. Atmospheric energy transport enables cloud shading and surface evaporation that cool the warmest waters. As the climate is warmed from the current temperature of the tropics, the processes that damp the SST contrast become stronger, making the oscillation in temperature contrast faster and weaker until the organized cycle of temperature contrast disappears altogether.

1. Introduction

The interactions among convection, circulation, and sea surface temperature (SST) in the tropics impact tropical storms, interannual variations in regional climate, the global energy budget of Earth, and the structure of climate change. The pattern and magnitude of tropical SST variations have been shown to affect the emergence of the global warming signal through its effect on clouds (Zhou et al., 2016). Specifically, low clouds over the cooler tropics will be more reflective if the tropical SST contrast increases, producing a negative pattern effect feedback (Andrews et al., 2018). In addition, the rate of warming over the warm pool in the western Pacific is important for global cloud feedback and regional climate responses, because the warm region has an effect on the global atmosphere (Dong et al., 2019). Therefore, understanding convection and SST interactions in the tropics and their role in controlling the SST contrast in the tropics are critical to estimating future warming and its impacts.

To study the thermodynamic interactions in a simplified setting, we employ a global aquaplanet climate model in which insolation is uniform, rotation is set to zero and the atmosphere interacts with a slab ocean model. Despite the lack of ocean dynamics in such a model configuration, the domain divides between warm convective regions and cooler subsiding regions in which the SST contrast is comparable to those observed within the Tropics (≈5K). If the heat capacity of the ocean is sufficient, these regions are robust and evolve slowly (Popke

et al., 2013; Reed et al., 2015). This aggregation has important effects on climate sensitivity by modifying the emission temperature (Pierrehumbert, 1995) and influencing the cloud properties (Bony et al., 2016). Mechanism denial experiments have shown that longwave feedbacks between clouds and water vapor are necessary to trigger self-aggregation (Bretherton et al., 2005; Tompkins & Craig, 1998; Wing et al., 2017), although details can differ across models and with global mean SST.

Hartmann and Dygert (2022) investigate the time-mean climate and its sensitivity in the simulations discussed here. In this paper, we seek to better understand the oscillations of this global climate about its mean state, which are characterized by variations in the global SST contrast, circulation, and climate feedbacks. In this way, we get a better view of the positive feedbacks that lead to growing SST contrast and the counteracting processes that damp SST contrast when it becomes large.

Coppin and Bony (2017) found that for mixed layer depths greater than about 10 m, their model exhibited cyclic variability with periods on the order of a year or more. They found a similar growth in the subsiding region and increase in the warm pool temperature that we find here, followed by a collapse of the warm SST values before beginning another cycle. They also noted that the global mean temperature decreases when the SST contrast is large. Drotos et al. (2020) investigate the cyclic behavior in the ECHAM6.3 model and find that the SST gradient builds a strong capping inversion in the subsiding region, which leads to an increase in low cloud fraction and a large global cooling event as part of the cycle. Coppin and Bony (2018), however, find that SST gradients actually limit the increase in low cloud cooling caused by self-aggregation alone.

Although these studies use general circulation models (GCMs), similar radiative-convective equilibrium experiments with ocean-mixed layers have also been conducted in cloud-resolving models. Tompkins and Semie (2021) found that interactive SST delayed the onset of convective aggregation, while Huang and Wu (2022) represented convective aggregation with interactive SST as a competition between the moisture convection feedback and the convection SST feedback. These feedbacks will play an important role here as well, although we focus less on the onset of convective aggregation and instead focus on the oscillation between aggregated and dis-aggregated states over a much longer timescale.

In this paper, we use the oscillation within the model to focus on the mechanisms that maintain the warmest SSTs and their potential impact on the SST pattern. We particularly focus on the role of the atmospheric energy transport between the rising and subsiding regions in constraining the SST contrast, and how this changes with warming. We find that the instability that leads to increasing SST contrast ends when atmospheric energy transport away from the warm region induces strong cooling of the warm SST by enhanced evaporation combined with shading of the surface by deep convective clouds. Simultaneously, a decrease in cloud fraction and evaporation occurs over the cooler regions. As the SST contrast increases and the subsiding region expands, the peak surface winds and evaporation move toward warmer SSTs. This reduces the low clouds over the coolest SST regions where subsidence of warm, dry air increases entrainment drying. Positive skewness of the SST distribution marks the period when transport efficiently cools the warm SST, low clouds decrease in the subsiding region, and the SST distribution returns to a more equable state.

The model and methods are described in Section 2 and an overview of the cycle is given in Section 3. The compositing procedure and results are described in Section 4 and Section 5 describes the changes in the oscillation as the SST is increased.

2. Model Experiments and Methods

The model used here is Geophysical Fluid Dynamics Laboratory's Atmosphere Model (AM2.1) with a slab ocean (Anderson et al., 2004; Delworth et al., 2006). The rotation rate is set to 0 and the insolation is globally uniform. CO_2 is set to 324 ppm and CH_4 to 1,650 ppb. Ozone is fixed to its tropical mean value. A horizontal spatial resolution of 2° latitude by 2.5° longitude, 32 vertical levels, and a time step of 900 s were used for the control experiments. A 50-m deep slab ocean is used. The diurnal cycle is included. These are the same simulations as described in Hartmann and Dygert (2022).

Seven experiments with incoming solar radiation corresponding to latitudes of 26, 28, 30, 33, 36, 38, and 45 at equinox will be discussed here. This yields four hot climates, two climates corresponding to the present-day tropics and a climate with the surface temperature of the present-day global average (289K; Table 1). Each

Table 1
Mean Values for Control Experiments

Case	SST	Tdif	Precip	SF	RH	OLR	Albedo
C289	288.7	6.10	2.83	0.58	48.9	234.7	0.24
C302	302.1	6.96	4.18	0.63	47.0	266.7	0.22
C304	303.5	8.03	4.46	0.65	46.0	271.5	0.22
C307	306.8	9.74	5.13	0.67	44.6	284.7	0.22
C309	309.2	11.14	5.60	0.67	43.6	295.1	0.22
C313	312.9	8.93	6.06	0.68	43.1	306.0	0.21
C318	318.4	6.29	6.39	0.75	42.8	317.3	0.19

experiment was run long enough to produce 40 years of stable climate for analysis after an initial spin-up period. These experiments are denoted by their approximate global average SST. For example, the control experiment with an insolation of 342 W m^{-2} is called "C302."

In addition to these control experiments, we performed two experiments in which surface enthalpy fluxes or atmospheric radiative heating rates throughout the column are homogenized horizontally. As seen in similar fixed SST experiments, making either the radiative cooling or surface fluxes uniform suppresses convective aggregation—greatly decreasing the SST contrast and its associated cyclic variability (Bretherton et al., 2005).

We will use an index of SST difference between warmest and coolest 20% of area (*Tdif*) to characterize the cycle and we will also divide the domain into subsiding and rising regions by using the mass average of the pressure velocity to define the subsiding regions and subsiding fraction (SF). We also use area averages over the regions of upward and downward motion.

To understand the energy transfer between the ascending and descending regions throughout the cycle, we will define the gross moist stability (GMS) to be the mass-integrated flux divergence of moist static energy (MSE). Our use of GMS is for convenience and to loosely tie our analysis to more rigorous and theoretical uses of the terminology (Neelin & Held, 1987; Raymond et al., 2009).

$$GMS = \frac{1}{g}\int_0^{P_s} \nabla \cdot (MSE\,\mathbf{V})\,dP \tag{1}$$

Here $\mathbf{V}$ is the horizontal velocity vector and P is the pressure. The units of GMS are W m^{-2}. We can compute the GMS point by point, and we can average over the area of rising motion. By using the GMS averaged over the region of upward motion (*GMSup*), we can measure how the circulation is influencing the energy balance in the upward region.

3. Overview of the Cycle

We center our analysis on the effects of the SST contrast and use the difference between the top and bottom 20% of SST, weighted by area, as our metric for describing the cycle and call it *Tdif*. By using the SST contrast as the compositing variable, we can look in more detail at how each component of the atmosphere varies with respect to the range of SST. This choice is to some extent arbitrary, since most quantities vary with the same period and all are coupled, but on fast time scales the atmosphere responds to the SST, so that we regard SST contrast as more of a control variable than SF, which, from a causality perspective, we will consider a response to the SST distribution. We will also consider composites of SF and skewness of the SST distribution.

To illustrate the degree of periodicity in the simulations, we show the power spectra of four variables in Figure 1. The temporal variance is proportional to the area under the curves. Most other variables, including the global mean precipitation and high cloud fraction, show similar changes in temporal behavior across the seven control cases. These spectra were computed with a Hamming window with a length of 64 months and 50% overlap from 480 months of model data, so each spectral estimate has a minimum of 15 degrees of freedom. Linear trends were removed from each segment before computing the spectra.

The spectra in Figure 1 show that the variance of SST contrast is very small for the cold case C289 and for the second hottest case C313. For the hottest case, C318, the variance increases again, but is more characteristic of white noise than a preferred period. A preferred period of about 30 months occurs for the intermediate cases, with the strongest variance for the cases that are similar to, or slightly warmer than, the present-day tropics. The frequency of the oscillation increases somewhat as the climate is warmed, and evidence of a higher harmonic appears as a side lobe to the main peak, notably for the energy export from the region of rising motion in the C307 case.

If starting from a uniform SST, random instability will result in convection that leads to a warming and moistening of the same region in which this convection is occurring. In regions without convection, radiative cooling will

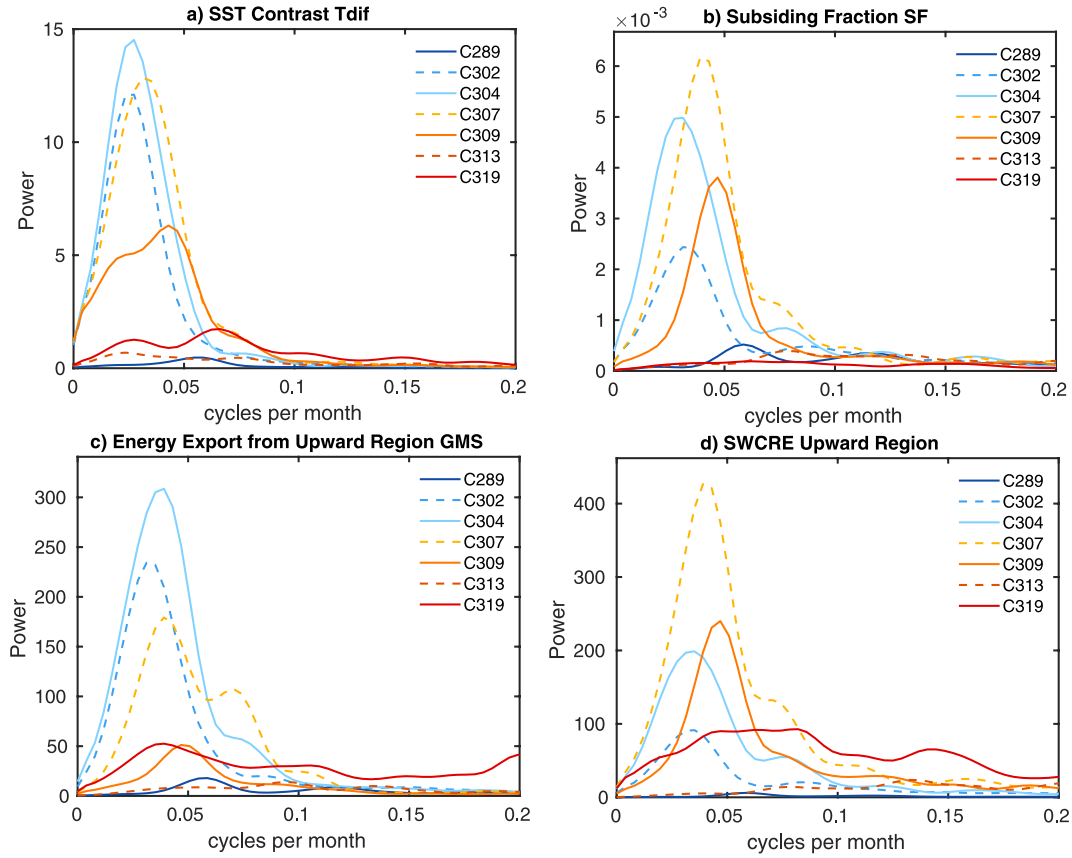

Figure 1. Power spectra for the seven control cases of (a) *Tdif*, (b) subsiding fraction (*SF*), (c) atmospheric energy export from the region of rising motion (*GMSup*), and (d) shortwave cloud radiative effect (SWCRE) in the region of upward motion.

support subsidence, drying of the free troposphere, and radiative cooling to balance convective heating elsewhere in the domain. The feedback between moisture, radiation, and circulation causes the domain to divide into regions with convection and regions of cooler SSTs with subsidence (Emanuel et al., 2014). The SST increases under the moist region and cools under the dry region. The SST distribution then cycles between times of low SST contrast and high SST contrast.

To illustrate the spatial structure of the oscillation, we show maps of the SST and low-level winds for case C304 in Figure 2. The scale of the SST contrast tends to assume the largest possible scale with one warm area and one cooler area. The cycle is illustrated with maps from the growing phase, the maximum contrast phase, the decaying phase, and the subsequent low-contrast phase when the SST is most equably distributed. Each phase is separated by about 8 months. During the growth phase, the SST distribution is negatively skewed and strong winds over the colder SST lead to an expansion of the cold region while the warm region maintains pockets of very high SST. In this particular case, as the cold region expands, winds weaken in the center of the cold region and the SST there begins to increase. Higher surface winds invade the warmer SST regions during the decay phase and the distribution of SST becomes positively skewed, with a relatively small region of very warm SST and a larger region of cooler SST. This evolves to the state of low SST contrast, at which time another cycle of SST contrast growth begins.

4. Compositing the Cycle

To understand how key variables change with SST, compositing of the cycle is performed relative to the parameter *Tdif*, the difference between the warmest and coldest 20% of SST by area. The time series of monthly *Tdif* values is first smoothed with a broad band-pass filter centered on the frequency in which the cycle has

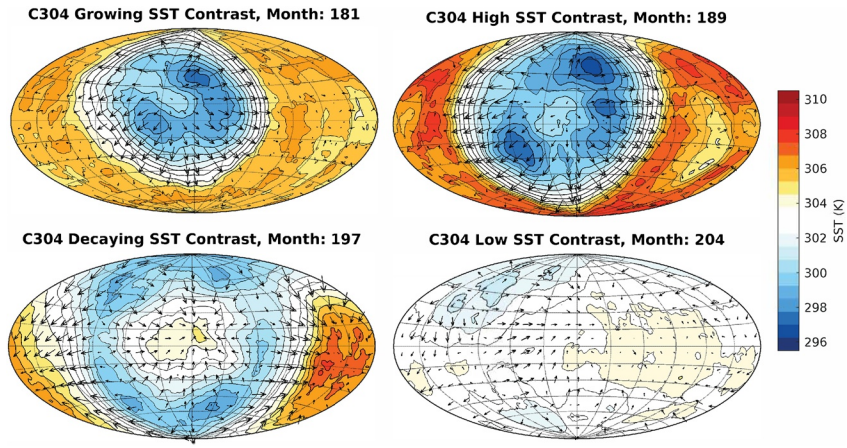

Figure 2. Monthly mean snapshots from one cycle of case C304 of sea surface temperature (SST) and reference-level winds at different stages in the SST contrast cycle: Growing, Maximum, Decaying, and Low SST contrast. Hammer equal-area projection is used.

the maximum amplitude. A sixth-order Butterworth band-pass filter with cuts at 0.04 and 0.02 of the Nyquist frequency was used on monthly data. The maxima of this time series then define the key dates for the compositing analysis, and a lagged compositing analysis is performed of the unfiltered variables of interest, so the filtering is only used to choose the key dates.

Diagnosis of the energy balances will be key to understanding the mechanisms of the cycle. Neglecting storage of energy in the atmosphere, energy balance requires that,

$$GMS = SWnet_{TOA} - OLR - SHB \tag{2}$$

where GMS is the net energy export by atmospheric transport, $SWnet_{TOA}$ is the net incoming solar radiation at the top-of-the-atmosphere (TOA), OLR is the outgoing longwave radiation, and SHB is the surface heat balance,

$$SHB = SWnet_{sfc} + LWnet_{sfc} - (LE + SH) \tag{3}$$

where SHB is also the energy storage in the ocean, $SWnet_{sfc}$ is the net solar absorption, $LWnet_{sfc}$ is the net longwave into the surface and LE and SH are the fluxes of latent and sensible heat away from the surface by turbulent motions.

Rearranging Equation 2, we can also write,

$$SHB = Rnet_{TOA} - GMS \tag{4}$$

where $Rnet_{TOA}$ is the net radiation balance at TOA. Equation 4 indicates the key role of atmospheric energy transport in controlling the surface heat balance. The trigger mechanism for strong atmospheric heat transport from the warm to the cool region will be shown to be a key determinant of the cycle. The atmospheric transport does not peak at the time of maximum SST contrast, but rather at a time determined by the positive skewness of the SST distribution and large SF. That the maximum atmospheric transport occurs after the time of maximum SST contrast and persists as the SST contrast decreases is critical to the oscillation.

Note here that our definition of the energy budget is an approximation based on the assumption that the atmospheric energy storage is small. On the time scale we are using here, atmospheric storage of energy is very small compared to the overall atmospheric energy transport. In addition, using GMS calculated directly by the definition given in Equation 1, rather than as a residual, does not alter our results.

4.1. Composites in SST Versus Time Space

We will first show the cycle in an SST histogram framework. Global data are binned by 0.25K SST increments for each monthly mean. These data are then composited relative to the time of maximum SST contrast. A probability

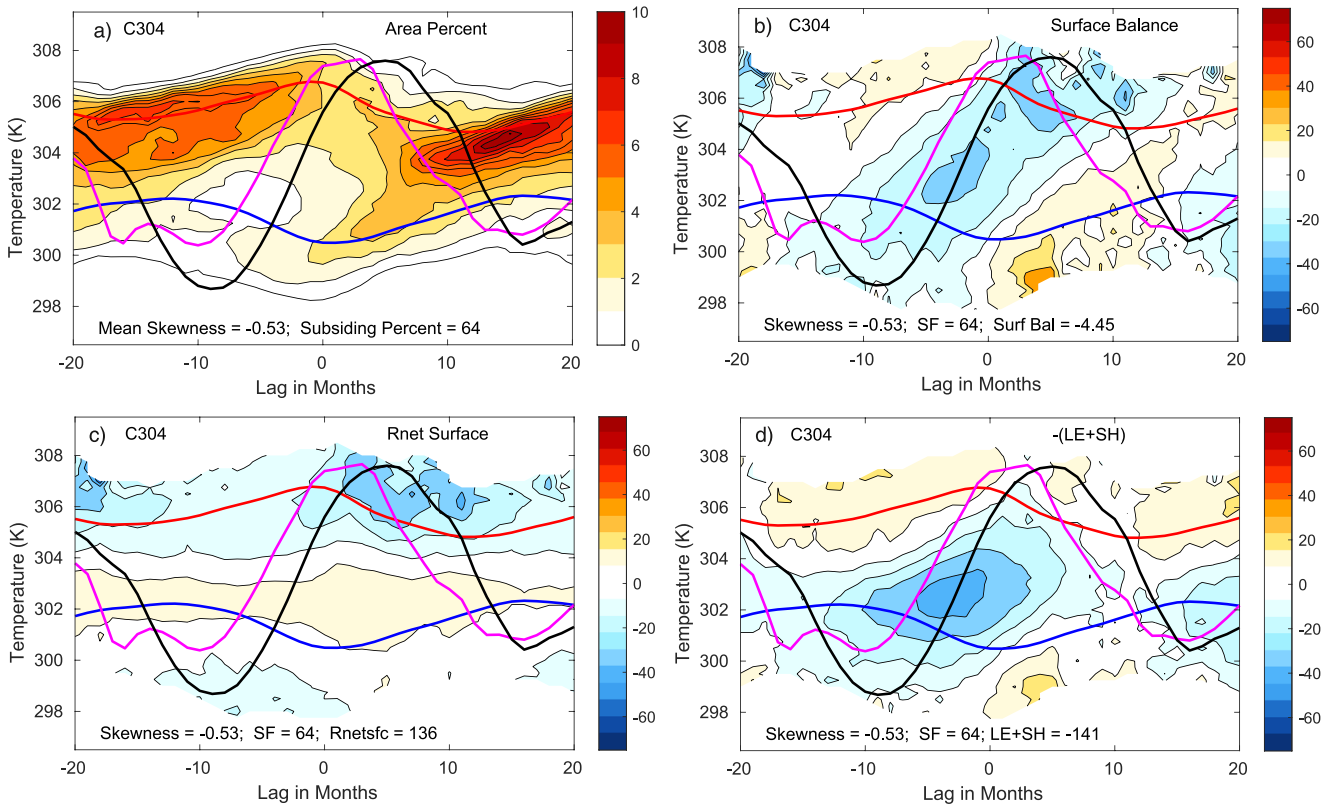

Figure 3. Composites of (a) sea surface temperature (SST) pdf in percent, (b) surface heat balance anomalies, (c) net surface radiation anomalies, and (d) surface turbulent cooling anomalies as functions of lag relative to the time of maximum SST contrast. Surface flux anomalies are in W m^{-2}. The red line represents the average of the top 20% of SSTs, while the blue line represents the bottom 20% of SSTs. The black line is the anomaly of the skewness of the SST pdf 10 times. The magenta line is the anomaly in the percent of the area that is subsiding. The values of subsiding fraction and skewness anomalies have an appropriate temperature added to them for plotting in the SST lag space.

distribution of SST can be formed at each lag by dividing the area-weighted number of hits in each SST bin by the total number of area-weighted hits.

Figure 3 shows composites of area percent and surface energy balance component anomalies as functions of SST and lag from the month of maximum SST contrast for case C304, Figure 3a can be found for all cases in Supporting Information S1. Minus lags are before and positive lags are after the maximum in *Tdif*. A contour of 10 for the pdf of area fraction means that 10% of the area is the same temperature to within 0.25K. The energy flux anomalies are from the unweighted average of all the values in the composite, which is given as text near the bottom of each panel. The actual values at each SST-lag point in the plot can thus be found by adding the mean to the contour value. This was done so that the magnitude of the anomalies in panels b–d can be plotted with the same contour interval to show the relative importance of the variations in different energy flux components, despite their very different mean values. Also shown as lines on these plots are the temperatures of the warmest and coolest 20% of area. Anomalies of the percent subsiding area and the skewness of the SST pdf (10 times) are also shown, plotted with an addition to make them appear within the diagram. The range of variation for each can be obtained from the temperature difference between the maximum and minimum of the curve, then dividing the skewness difference by 10. So the range of skewness over the cycle in Figure 3 is about 0.9 and the range of SF is about 7%.

Figure 3a shows that 10 months before the maximum *Tdif*, most of the domain is covered by warm SSTs of a nearly uniform value. This warm region warms further, but decreases in area coverage as a region of cool SST develops that is about 6K colder than the warm pool. This trend continues until at maximum *Tdif* the pdf is bimodal, positively skewed, and the subsiding area fraction is approaching its largest value. After maximum *Tdif* is reached, shortwave cloud shading and enhanced evaporation strongly cool the surface of the warm region, and decreased evaporative cooling warms the cold region. By 10 months after maximum *Tdif*, a new warm pool has formed at a cooler temperature and the process repeats.

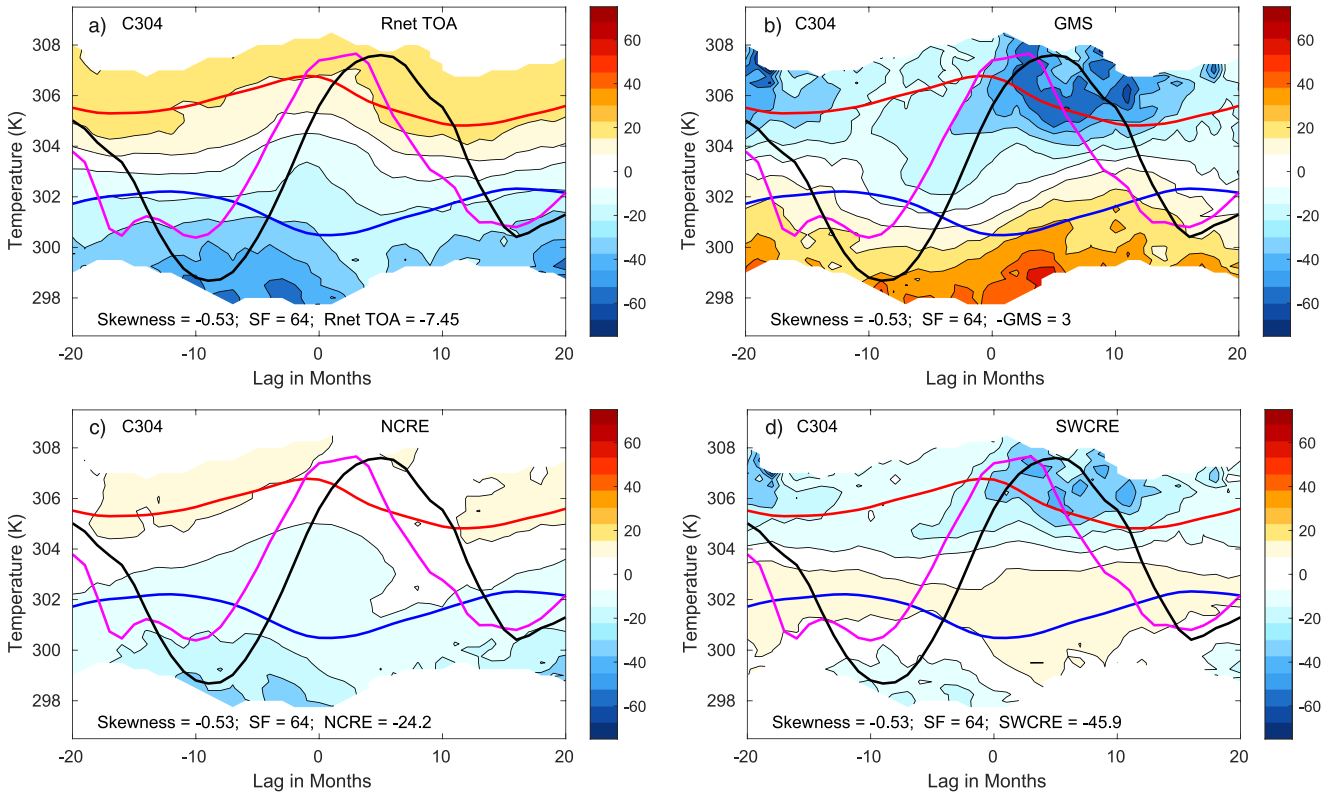

Figure 4. As in Figure 3 except, (a) net top-of-the-atmosphere (TOA) radiation anomaly, (b) -GMS net atmospheric energy export anomaly plotted with negative sign, (c) net cloud radiative effect anomaly, and (d) shortwave cloud radiative effect anomaly.

Figures 3b–3d show the anomalies in the surface energy budget terms. A region of negative net heat balance propagates from the cold to the warm SSTs as *Tdif* approaches and then passes its maximum value (lag 0). Surface turbulent and cloud radiative effects collaborate at the extremes of SST distribution with radiation dominating the variation at high temperatures and surface turbulent flux variations dominating at low temperatures. The effect of low clouds in the cool region is weaker than in some other simulations, notably Drotos et al. (2020).

Figure 4 shows TOA energy budget quantities and GMS, the convergence of atmospheric energy transport in W m^{-2}. The net radiation and net cloud radiative effect (NCRE) vary little over the warmest water during the cycle, in general agreement with a weak NCRE in observations (Harrison et al., 1990). A mechanism to keep TOA NCRE small in a climate model with a mixed layer has been tested by Wall et al. (2019). Atmospheric transport and shortwave cloud radiative effect cool the warm region strongly during the period when the temperature of the warmest water is declining (Figures 4b and 4d). SWCRE is mostly offset by LWCRE at TOA, but the enhanced export of energy by atmospheric transport facilitates the cooling of the surface, as atmospheric energy export is balanced by enhanced evaporative cooling of the surface (Equation 4). NCRE anomalies become significantly negative over the coolest regions, but these cool regions occupy a very small fraction of the total area. The proximate cause of the strongest cooling of warm SST is marked by a strong increase in atmospheric export, which peaks after the maximum SST is achieved and continues until the SST distribution is at its most equable. This atmospheric energy export is correlated with positive skewness of the SST distribution.

To summarize the section,

1. The SST gradient grows in the beginning of the cycle as low clouds and surface evaporation cool the subsiding region and the greenhouse effect warms the ascending region.
2. As the SST contrast grows, the SF and area of coldest SST grow. The shrinking warm pool and expanding cold pool are represented by the increasing skewness of the SST distribution.
3. The increasing skewness of the SST distribution then leads to a strong increase in atmospheric energy transport away from the warm pool.

4.2. Streamfunction Composites

In the previous section, it was shown that atmospheric transport of energy plays an important role, especially during the time when the warmest SST values are cooling rapidly. In this section, we will investigate the circulation between the warm and cool areas using a streamfunction. Hartmann and Dygert (2022) binned the model data by SST and plotted the data by the fraction of the area occupied by SST from coldest to hottest. Since the coordinate is then proportional to area, we can compute and plot a streamfunction as a function of pressure in this coordinate system. This reveals that the overturning circulation has two circulation cells, a lower one that is tied to surface processes and the decline of humidity above the boundary layer, and a deep circulation that is driven by the heating and cooling in the upper troposphere and tends to remain at a fixed temperature as the climate is changed. In Figures 5a, 5e, 5f, 5m, and 5q, we show these streamfunction plots for the prior weak, growth, maximum, decay, and posterior weak gradient phases of the SST contrast for case C304.

During the time when the SST contrast is increasing fastest (Figures 5e–5h), the lower and upper circulation cells are centered in the relatively cool SST region with a narrow region of subsiding motion over the cool SST and a broad region of weak upward motion over the warmer SST. The shallow circulation is stronger than the deep circulation cell. The net heating rate (Figure 5f) that balances the shallow circulation is driven by radiative cooling over the coolest SSTs with a relatively shallow convective heating over the intermediate SST values. Low fractions of high cloud extend across the warmest 60% of SST area (Figure 5g) and the region of low mid-tropospheric relative humidity is confined to a small region of low SST values. A sharp decline in relative humidity occurs near the top of the boundary layer (Figure 5h). A maximum in the relative humidity occurs in the lower troposphere at intermediate values of SST, and is associated with the upward branch of the shallow circulation. The growth phase is thus composed of a small area of intense downward motion and a larger area of weak upward motion and relatively thin, but widespread high cloud. The downward motion is especially strong in the lower troposphere, where it is driven by radiative cooling at the top of the boundary layer and in the air above, which becomes drier with altitude. This shallow circulation driven by radiative cooling at the top of the boundary layer is consistent with the radiatively driven large-scale instability that separates the flow into rising and subsiding regions described by Emanuel et al. (2014), except that it is limited to a shallow circulation.

As the cycle progresses toward maximum SST contrast at lag = 0 (Figure 5i–5l), the lower and upper circulation cells both strengthen and move toward warmer SST as the downward region expands in area and the upward motion over the warmest SST increases in strength. The center of the lower overturning cell moves from 0.3 to 0.5 SST area fraction, compared to the growth phase. The diabatic heating and the relative humidity distributions also shift consistently with the overturning circulation. The radiative cooling associated with the wedge of low humidity that extends into a larger area toward warmer SST helps to balance the subsiding motion in the more intense lower cell.

These trends continue into the phase of most rapid SST decline (Figure 5m–5p). In this phase, the diabatic heating and high cloud amount are concentrated over the warmest SST and the vertical velocity reaches a maximum over the highest SST. This phase is associated with a maximum in the export of energy from the warm region (Figure 4b), which results in the rapid cooling of the warm SST waters by evaporative cooling and shortwave shading.

The cooling phase has sufficient momentum to return the SST distribution to a nearly uniform warm pool about 14 months after the maximum SST difference was attained (Figure 3a). The SST distribution is more uniform after the maximum in *Tdif* than before it. With a relatively weak SST difference, the circulation is weak, but the small region of subsiding motion exists and is ready to develop into another cycle of increasing SST contrast (Figure 5q). This low-contrast phase has a large area with high clouds and a relatively small area where low humidity extends down to the boundary layer (Figures 5s and 5t).

The circulation throughout the cycle, as described above, develops as follows:

- Toward the beginning of the cycle, just as the SST gradient and the moisture gradient across SSTs begin to increase, a strong shallow circulation develops over the coldest SSTs. This shallow circulation is associated with the drying of the troposphere in the region of subsiding motion and is in turn enhanced by the radiative cooling from the boundary layer.
- As the subsiding region expands, the warm pool shrinks, and convection intensifies; both the shallow and upper circulation cells shift to warmer SSTs.

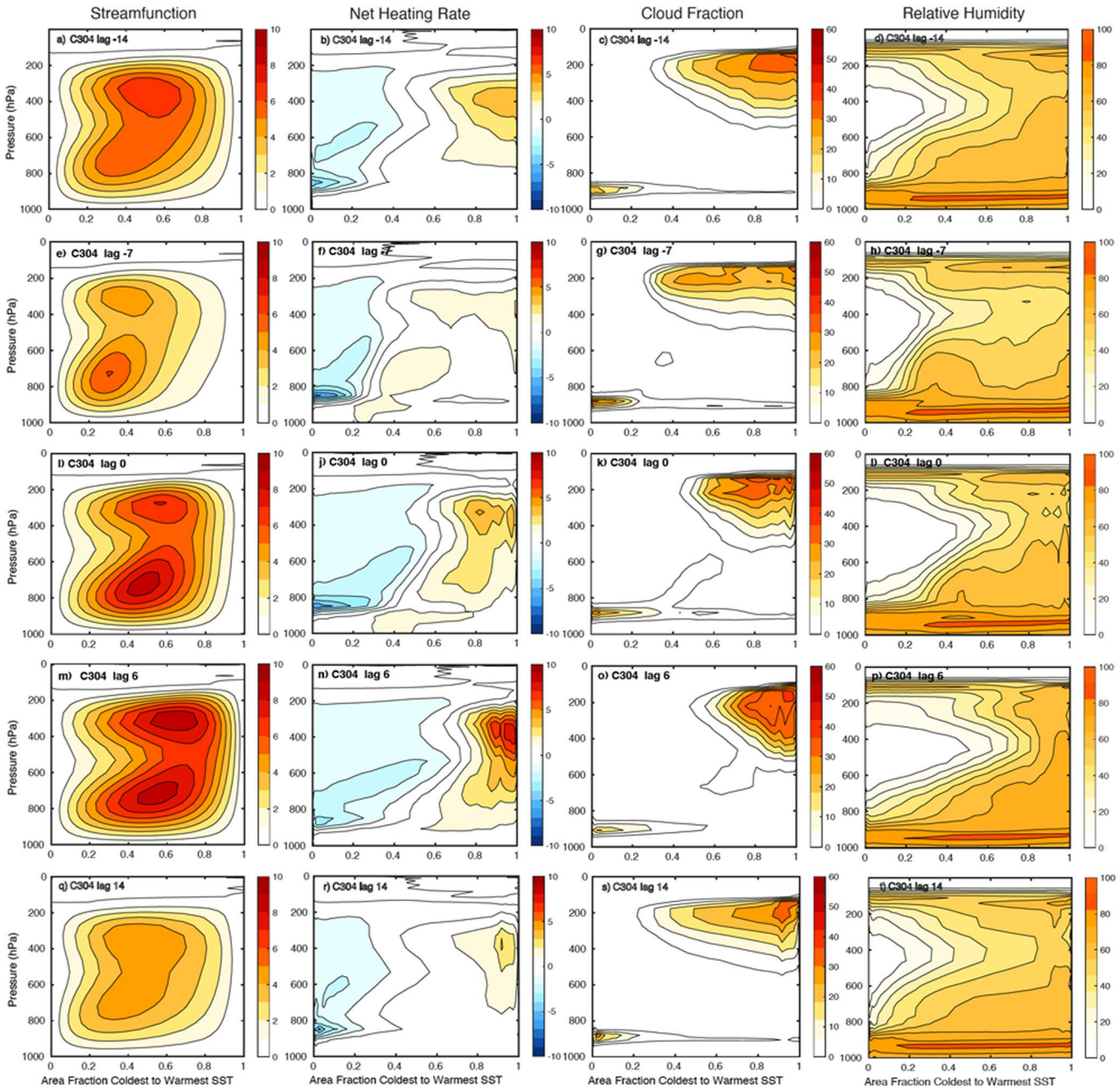

Figure 5. Streamfunction (10^{11} kgs^{-1}), diabatic heating rate (Kday^{-1}), cloud fraction (%), and relative humidity (%) as functions of pressure and sea surface temperature (SST) area fraction for the preceding small gradient phase (lag = −14, a–d), growth phase (lag = −7 months, e–g), maximum SST contrast (lag = 0, i–l), decay phase (lag = +6 months, m–p), and proceeding small gradient phase (lag = +14, q–r).

- As the circulation peaks over the warmest SSTs, the resulting increase in export of energy from this region helps bring the SST distribution back to its original, relatively uniform distribution.

4.3. Compositing of Upward and Downward Regions

In this section, we consider composites of averages of the energy budget quantities over the rising and subsiding regions. Figure 6 shows top-of-atmosphere and surface energy budget composites for averages of the upward and downward regions for case C304. These are plotted as anomalies from their time mean values. We include the -GMS term with the TOA radiative fluxes to indicate the important role of atmospheric transport in the cycle.

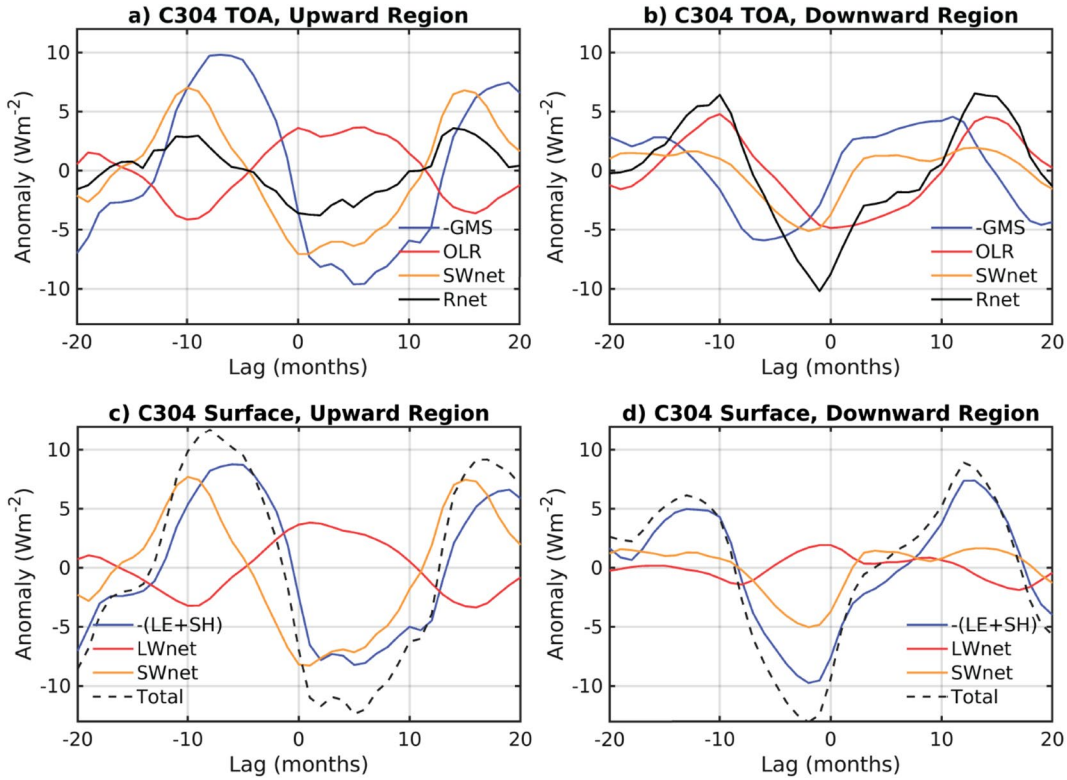

Figure 6. Anomalies in each term of the top-of-the-atmosphere (TOA) (a, b) and surface energy (c, d) budgets for the upward and downward regions for case C304.

The atmospheric transport term (-GMS) has the largest variation of all the terms in the upward region for the top of the atmosphere energy balance (Figure 6a). At the surface in the upward region (Figure 6c), the turbulent heating term -(LE + SH) has almost exactly the shape of the atmospheric energy export, which is required by the atmospheric energy balance.

The atmospheric transport and net shortwave radiation (SWnet) both act to increase *Tdif* when it is increasing and reduce it when it is decreasing. The longwave term (-OLR) has smaller variations during the cycle and acts to decrease the amplitude of the cycle of *Tdif*. Interestingly, SWnet in the upward region peaks early in the cycle of growth when *Tdif* is at a minimum (∼−10 months), declines as *Tdif* grows and then becomes negative before *Tdif* reaches its maximum value at lag 0. This suggests that the SWCRE is playing an important role in controlling the cycle, since it is the first term to reverse direction in the upward region as the cycle progresses.

At the surface in the downward region, the turbulent cooling and cloud shading contribute to the cooling leading up to maximum *Tdif*, while the LWnet plays a weaker role. The heating anomalies do not become substantially positive until more than 10 months after the maximum *Tdif*, when the surface anomalies in the upward region have also returned to positive anomalies (compare Figures 6c and 6d).

4.4. Low Clouds Through the Cycle

The low clouds in the subsiding region also show significant changes throughout the cycle. As shown in Figure 7a, over the coldest SSTs, the low cloud fraction increases as the SST contrast grows before dropping sharply just as the SST contrast peaks. The second, smaller low cloud maximum over intermediate SSTs is associated with convection and low-level convergence as the subsiding region expands, and so is explained by a different mechanism from the main low cloud peak over the coldest SSTs. From previous studies, we would expect this low cloud decline to correspond to a decline in inversion strength. However, in this model, low clouds begin to decrease while inversion strength is still increasing, as shown in Figure 7c. So, another explanation is required here.

Instead of EIS, we find that clear sky longwave cooling best explains the onset of the low cloud decline. We focus on clear sky longwave cooling at 880 hPa, where the cloud fraction is maximized, shown in Figure 7b. To

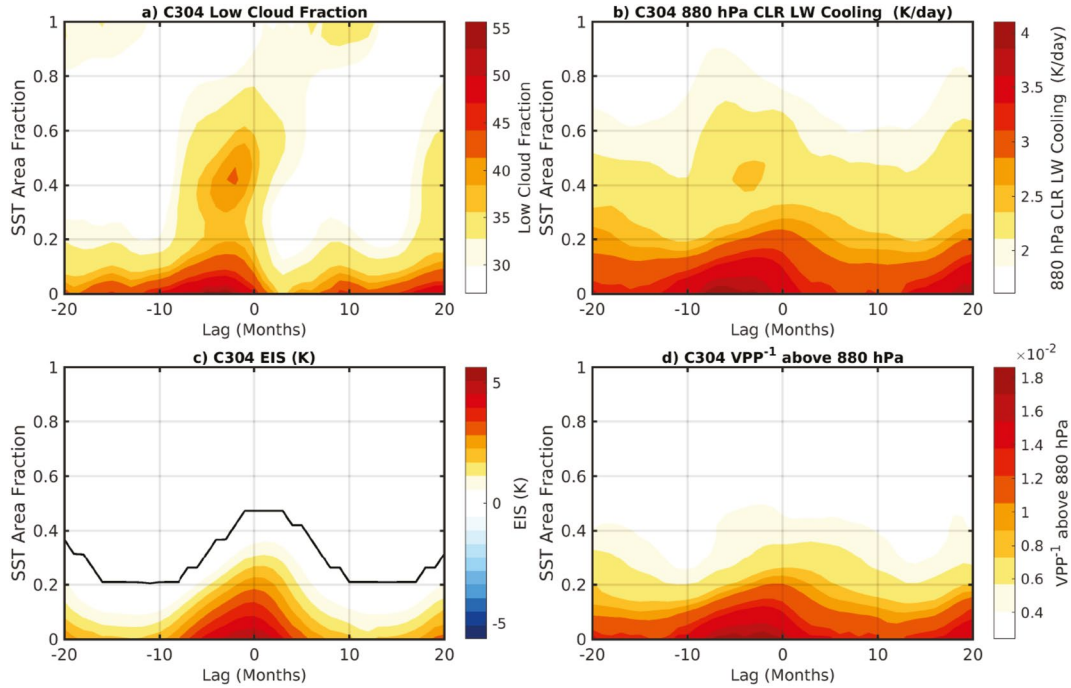

Figure 7. Lagged composites of variables in sea surface temperature (SST) area fraction coordinates for case C304, showing (a) cloud fraction, (b) clear sky longwave cooling at 880 hPa (Kday^{-1}), (c) estimated inversion strength, EIS (K), and (d) the inverse of vapor pressure path (VPP).

understand this decrease in longwave cooling, we turn to the cooling-to-space approximation. The derivation of the form used here can be found in Hartmann et al. (2022).

$$\left.\frac{dT}{dt}\right|_{\lambda} \approx -\left\{\frac{e^{-1}\,\pi\, g}{c_p}\, RH\; e_s(T)\; B_{\lambda}(T)\right\} VPP^{-1}. \tag{5}$$

where

$$VPP = \int_0^p RH e_s(T) dp \tag{6}$$

From these equations, we know that the clear sky longwave cooling rate is proportional to the vapor pressure at the level of emission and inversely proportional to the vapor pressure path (VPP) above that level. The inverse of VPP above 880 hPa is shown in Figure 7d. Especially over the coldest water, it decreases in phase with the clear sky longwave cooling rate at 880 hPa shown in panel b. We find that the change in VPP above 880 hPa appears to be the main contributor to the change in the clear sky longwave cooling rate.

The VPP is determined by both relative humidity and temperature, the lagged composites of which are shown in pressure coordinates for the downward region in Figure 8, panels b and c. In Figure 8a, cloud fraction is shown in pressure coordinates for comparison with the relative humidity and temperature changes. Due to the large-scale circulation, the air temperature in the subsiding region is set by the surface temperature in the ascending region. As the hottest SSTs warm, so does the tropospheric air temperature in the subsiding region. So, with temperature increasing, we would expect an increase in VPP as the SST contrast grows, and a decrease as it decays, if the relative humidity is fixed. This is the opposite of what we see, however. The relative humidity decrease from subsidence drying wins out over the temperature increase, and the VPP decreases as the contrast grows, reaching a minimum just before the peak SST contrast.

While the VPP is set by the relative humidity changes, the increase in relative humidity above the boundary layer clouds just before the SST contrast peaks is set by changes in the circulation. Section 4.2 describes the changing circulation throughout the cycle, and Figure 5 shows the peak of the shallow circulation moving to warmer

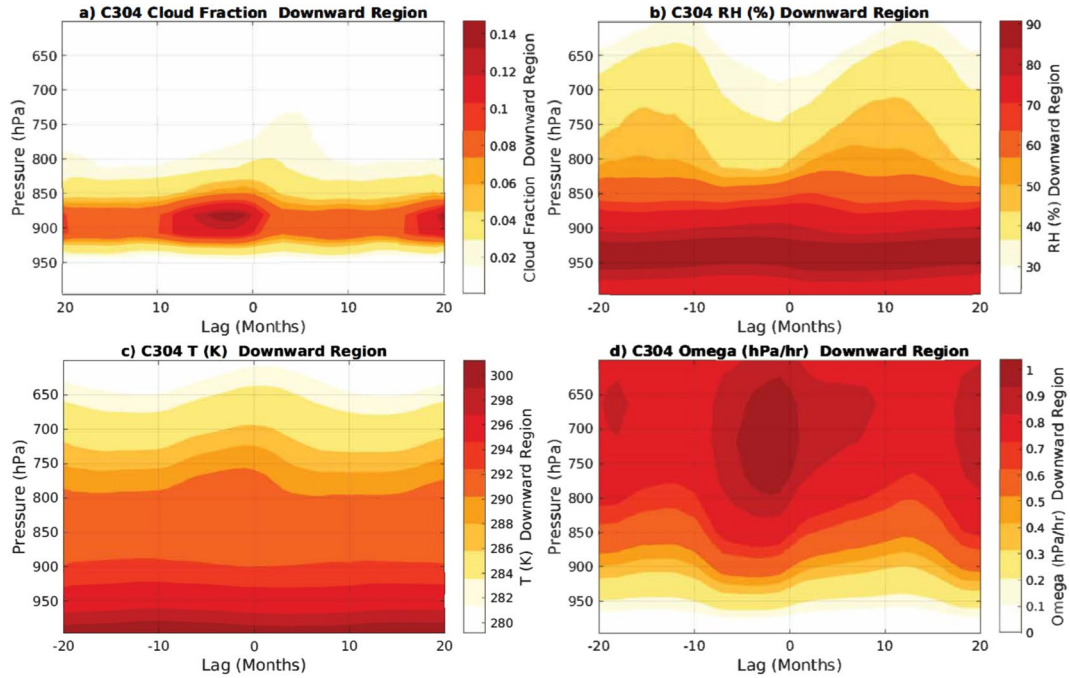

Figure 8. Lagged composites of variables in pressure coordinates averaged over the region of downward motion for case C302, showing (a) cloud fraction, (b) relative humidity (%), (c) temperature (K), and (d) vertical motion (hPa/hr).

SSTs as the cycle progresses. The overall effect of this migration is illustrated in Figure 8 which shows the time evolution of vertical profiles key to understanding changes in cloud fraction and relative humidity. As the SF expands and the shallow circulation moves toward warmer SSTs, the subsidence over the boundary layer begins to decrease, as shown in Figure 8d. Working alone, we would expect this decrease in subsidence above boundary layer clouds to increase the low cloud fraction (Bretherton & Blossey, 2014). Decreased subsidence increases low cloud amount by allowing for deeper inversions, weaker entrainment, and an increased vertical extent of boundary layer clouds. However, in this model, the strong, large-scale organization of convection results in most of the water vapor in the free troposphere concentrated over areas of convection, leading to low relative humidity (around 40%) above the boundary layer in the subsiding region. So, when subsidence drying above the boundary layer weakens, this results in an increase in relative humidity, but an insufficient increase to promote cloud growth. Instead, the increased humidity above the boundary layer sharply decreases longwave cooling, cutting off radiatively driven turbulence necessary to sustain the boundary layer clouds.

The secondary peak of low clouds near SST area fraction of 0.4 in Figure 7a similarly depends on the shallow circulation cell moving into warmer SSTs. As the SST contrast peaks, the subsiding region expands, and the vertical velocity over intermediate SSTs flips from upward to downward motion (Figures 5e–5m). This transition to downward motion leads to the rapid decrease in the low cloud fraction. Over these intermediate SSTs, the maximum cloud fraction in pressure coordinates occurs in the middle troposphere (Figures 5f and 5g), suggesting that this secondary maximum of low clouds is associated with the congestus mode of convection (Nuijens & Emanuel, 2018).

To summarize this section, cloud fraction over the coldest SSTs sharply decreases, starting just before the SST contrast peaks. This coincides with a decline in clear sky longwave cooling at the level where low clouds are maximum, 880 hPa. This decline in longwave cooling is primarily explained by an increase in VPP above 880 hPa, which itself comes from a decrease in subsidence. Over intermediate SSTs, low clouds associated with the congestus mode of convection similarly decline as the subsiding region expands.

5. Modification of the Cycle With Mean SST

We have described the mechanisms of the cycle for case C304 due to its resemblance to the current tropics as well as the robust cycle it exhibits. As shown by the power spectra in Figure 1, the cycle is strong for cases C302,

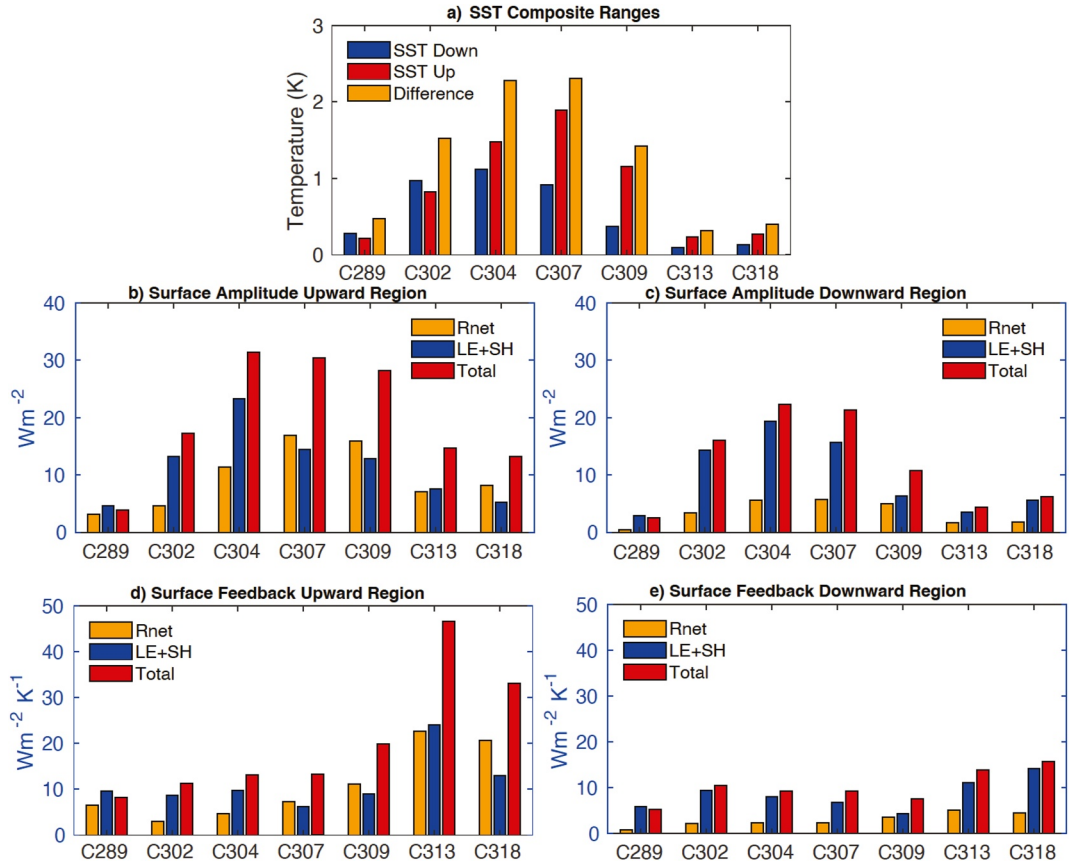

Figure 9. (a) Peak-to-peak amplitude of the sea surface temperature (SST) cycles in the upward and downward regions and of the difference between the upward and downward regions. Peak-to-peak amplitude of surface energy component composites in the (b) upward and (c) downward regions, and the feedback obtained by dividing the peak-to-peak amplitude of the energy budget quantities by the amplitude of the difference between the upward and downward SST for the (d) upward and (e) downward regions.

C304, and C307. For case C309, the cycle speeds up, and for the warmest cases, C313 and C318, the cycle is either weak or chaotic. Here, we wish to better understand why these changes in variability of the model climate occur as it is warmed above the temperature of the current tropics. Our hypothesis will be that the strengths of the energetic and hydrologic feedbacks increase so that small variations in SST are met with a strong reaction that limits the cycle amplitude. This is consistent with the reduction in the mean SST difference with warming for the mean climate shown in Hartmann and Dygert (2022). In addition, SF and SST skewness both increase with SST, and these changes both enhance the effectiveness with which atmospheric transport can cool the warm region and decrease the effectiveness of strong subsidence in drying the cold region.

5.1. Feedback Strength and Warming

We can estimate the strength of the response of components of the energy budget to the SST contrast by using the peak-to-peak cycle amplitudes from the composites such as those shown in Figures 3, 4, and 6, from which the SST and energy budget components in the upward and downward regions can be computed. To estimate the peak-to-peak amplitude, we first smooth the composites with a 1-2-1 filter to reduce the effects of noise. Figure 9a shows bar chart plots of the peak-to-peak amplitude of the SST in the upward and downward regions and of the difference between the upward and downward regions. The amplitude of the cycle in the difference between the upward and downward regions at first increases and then decreases for the three warmest cases. As the SST is warmed, the amplitude of the difference is increasingly dominated by the changes in the region of upward motion. The reduction in the cycle at high temperatures may be related to the decline in the mean SST difference. In Hartmann and Dygert (2022), it was shown that the decline in the mean SST difference between upward and

downward regions at warm temperatures is related to a decline in the contrast in the greenhouse effect between moist and dry regions.

Figures 9b and 9c show the amplitude of the cycles in the surface energy budget for the upward and downward regions, respectively. These also increase and then decrease as the SST is warmed. Figures 9d and 9e show the feedback estimated by dividing the amplitude of the surface energy budget cycles by the amplitude of the cycle in the SST difference between the upward and downward regions. The goal here is to estimate how sensitive the flux cycles are to the SST difference cycle. We see that for the warmest cases, the feedback gets larger, especially in the upward region. This suggests that as the SST warms, the energy balance terms become much more sensitive to the SST and that this is what suppresses the magnitude and organization of the cycle. The relative importance of radiation feedbacks compared to latent cooling feedbacks increases from the cooler to the warmer climates in the upward region, but not in the downward region.

From this section, we see that the strength of the oscillation is closely tied to the strength of the hydrologic cycle. Although the SST contrast, in its mean state, peaks in case C309, we see that the cycle magnitude has already begun to decline. This decline and eventual disappearance of the cycle is shown to correspond to the strengthening of negative feedbacks with increasing global mean SST.

6. Summary and Conclusion

Global climate models in tropical aquaplanet mode with no rotation, uniform insolation and a slab ocean typically exhibit sustained oscillations about their climatological mean state. These oscillations can be characterized by the variations in the difference between the warmest and coolest quantiles of SST, by the difference in SST below the regions of upward and downward mean atmospheric motion or by the fraction of the global area that is rising or subsiding. For mean SST values close to the current tropics, the climatological SST distribution is negatively skewed with a large area of nearly uniform warm SST and smaller regions with much cooler SST, as in the observed tropics (Hartmann & Dygert, 2022).

Starting from a state of near uniform SST, the SST contrast grows because the energy balance is positive over the warmer regions and negative over the cooler SST regions, most fundamentally because of the enhanced water vapor greenhouse effect in the convective region over the warmest SSTs. Subsidence over the cool region causes drying of the free troposphere, and the radiative cooling near the top of the boundary layer drives a shallow circulation that enhances the evaporation near the boundary between the warm and cool SST. The warmer water thus continues to warm, and a circulation develops that cools the SST outside the convective region via enhanced surface winds and reduced relative humidity. As the SST contrast grows, the export of energy from the warm area by atmospheric transport becomes more efficient so that the warm area becomes smaller, while the area of cooler SST expands.

When the SST contrast reaches its peak value, the cool area has grown and the warm area has shrunk to the point that the distribution of SST is positively skewed. This condition leads to efficient atmospheric transport of energy out of the warm region. Export of energy by atmospheric transport is associated with strong cooling of the warm region SST by cloud shading and enhanced evaporative cooling. The continued cooling of the warm region has more to do with the distribution of SST rather than the SST contrast, and is most efficient when the warm SST occupies a smaller fraction of the domain. This cooling of the warm region continues as the SST contrast declines and returns the SST distribution to a more uniform state with the pdf of SST peaked at an intermediate value.

Changes in the warm region are complemented by changes in the subsiding region, where the low cloud amount declines rapidly after the maximum SST contrast is achieved, helping the cool region to warm. The warm and cool regions are connected by atmospheric transport, which moves energy from the warm to the cool region most effectively during the period of rapid decline in SST contrast. Atmospheric energy export from the warm region is necessary to support the evaporative cooling of the surface there when the SST contrast is in decline. The cycle then repeats after the SST distribution becomes more equable and the positive feedbacks that lead to increased SST contrast begin again.

The cycle of low clouds differs slightly from Drotos et al. (2020) in that the inversion strength peaks after the low clouds have already begun to decline. Instead, we link the sharp decline in low clouds to the water vapor path above the boundary layer, which is set by the circulation. We find that the decreased magnitude of subsidence as

the subsiding region expands leads to an increase in water vapor above the boundary layer. Because the convective aggregation significantly dries the free troposphere in the subsiding region, this increase in relative humidity is not sufficient to increase cloud water at smaller pressure levels. Instead, the increase in water vapor above the boundary layer decreases clear-sky longwave cooling across the cloud top. The decrease in radiatively driven turbulence results in a sharp decline in cloud fraction.

Evaporation and SW shading remain the dominant mechanisms for driving the cycle as the climate is warmed, but their relative contributions and oscillation amplitudes change with warming and also between regions of upward and downward motion within the same experiment. In the subsiding region, evaporation consistently plays a larger role than SW shading by as much as a factor of 2 for the colder cases. In the ascending region, however, evaporation and SW shading contribute approximately equally. SW shading becomes relatively more important in the rising region in warmer climates.

The coherence and amplitude of the oscillation vary with mean SST. For climates colder than the current tropics, the oscillation is very weak and constrained to the regions of warmest SST. For climates substantially warmer than the current tropics, the oscillation first speeds up and weakens and eventually disappears for very warm climates. The reasons for this have to do with the distribution of SST and the strength of the hydrologic and energetic feedbacks. For warmer cases, the mean skewness of the SST distribution becomes positive, a situation in which the large-scale circulation acts to quickly suppress the growth of the warm SST regions. Also, the negative feedbacks become much stronger in a warmer climate. We measure the strength of the feedbacks by comparing the amplitude of the surface energy budget variations with the amplitude of the SST contrast between the upward and downward regions. For warmer cases, a small increase in the SST contrast results in a much larger change in the energetic responses, which suppress SST contrast and its variations. These feedbacks are especially strong in the region of upward motion and warm SST, so that small increases in warm pool SST are met with large increases in shortwave cloud shading and evaporative cooling.

To summarize the main conclusions,

1. Atmospheric transport of energy between the rising and subsiding regions is critical for the development of warm SSTs. As the SST contrast builds and the circulation increases, the cooling of the warm pool is marked by a large export of energy into the subsiding region.
2. The sudden decay of low clouds over the coldest SSTs is driven by a sharp decline in clear sky longwave cooling due to increased vapor above the boundary layer clouds. This increased water vapor is associated with a decrease in subsidence drying as the subsiding region expands.
3. The oscillation speeds up as global mean SST increases, until the signal disappears for cases warmer than 309K. This increase in cycle speed is associated with increased efficiency of damping hydrologic feedbacks at warmer temperatures.

Some of the model behavior discussed here may be sensitive to the particular parameterizations employed in the model and so should be tested in different GCMs. The basic behavior of this model is very similar to the behavior discussed by Coppin and Bony (2017), however, and the key role of radiative contrasts between the upward-wet and downward-dry regions is robust and fundamental. The special role of the shallow circulation driven by radiative cooling in the subsiding region in driving the cycle of SST contrast appears to be a novel and likely robust result of this analysis.

The relative importance of feedbacks in the rising and subsiding regions is particularly sensitive to the parameterizations of ice clouds and low clouds, respectively. Simulations with models with sufficient resolution to not require a cumulus parameterization would be particularly interesting, but those simulations would also be sensitive to the ice cloud microphysics parameterization and the boundary layer cloud parameterizations. Moreover, the simulation of tropical anvil clouds is critical, since they contribute most of the radiative effect of tropical convective clouds, and even higher resolution may be necessary to simulate the dynamical, radiative, and cloud-physical interactions within the anvils (Gasparini et al., 2019; Hartmann et al., 2018).

The SST contrast in the real tropics certainly depends on the effect of rotation and ocean heat transport. The way that these interact with the physical processes described here can be studied in future work.

Data Availability Statement

Model data used in this study can be accessed here: http://hdl.handle.net/1773/46293 (Dygert & Hartmann, 2022).

Acknowledgments
This work was supported by NSF Grants AGS-1549579 and AGS-2124496. The GCM code was provided by the NOAA Geophysical Fluid Dynamics Laboratory. Anonymous reviewers provided useful suggestions that improved the paper.

References

Anderson, J. L., Balaji, V., Broccoli, A. J., Cooke, W. F., Delworth, T. L., Dixon, K. W., et al. (2004). The new GFDL global atmosphere and land model AM2-LM2: Evaluation with prescribed SST simulations. *Journal of Climate*, *17*(24), 4641–4673.

Andrews, T., Gregory, J. M., Paynter, D., Silvers, L. G., Zhou, C., Mauritsen, T., et al. (2018). Accounting for changing temperature patterns increases historical estimates of climate sensitivity. *Geophysical Research Letters*, *45*(16), 8490–8499. https://doi.org/10.1029/2018gl078887

Bony, S., Stevens, B., Coppin, D., Becker, T., Reed, K. A., Voigt, A., & Medeiros, B. (2016). Thermodynamic control of anvil cloud amount. *Proceedings of the National Academy of Sciences of the United States of America*, *113*(32), 8927–8932. https://doi.org/10.1073/pnas.1601472113

Bretherton, C. S., & Blossey, P. N. (2014). Low cloud reduction in a greenhouse-warmed climate: Results from Lagrangian LES of a subtropical marine cloudiness transition. *Journal of Advances in Modeling Earth Systems*, *6*(1), 91–114. https://doi.org/10.1002/2013MS000250

Bretherton, C. S., Blossey, P. N., & Khairoutdinov, M. (2005). An energy-balance analysis of deep convective self-aggregation above uniform SST. *Journal of the Atmospheric Sciences*, *62*(12), 4273–4292. https://doi.org/10.1175/JAS3614.1

Coppin, D., & Bony, S. (2017). Internal variability in a coupled general circulation model in radiative-convective equilibrium. *Geophysical Research Letters*, *44*(10), 5142–5149. https://doi.org/10.1002/2017GL073658

Coppin, D., & Bony, S. (2018). On the interplay between convective aggregation, surface temperature gradients, and climate sensitivity. *Journal of Advances in Modeling Earth Systems*, *10*(12), 3123–3138. https://doi.org/10.1029/2018MS001406

Delworth, T. L., Broccoli, A. J., Rosati, A., Stouffer, R. J., Balaji, V., Beesley, J. A., et al. (2006). GFDL's CM2 global coupled climate models. Part I: Formulation and simulation characteristics. *Journal of Climate*, *19*(5), 643–674. https://doi.org/10.1175/jcli3629.1

Dong, Y., Proistosescu, C., Armour, K. C., & Battisti, D. S. (2019). Attributing historical and future evolution of radiative feedbacks to regional warming patterns using a Green's function approach: The preeminence of the Western Pacific. *Journal of Climate*, *32*(17), 5471–5491. https://doi.org/10.1175/JCLI-D-18-0843.1

Drotos, G., Becker, T., Mauritsen, T., & Stevens, B. (2020). Global variability in radiative-convective equilibrium with a slab ocean under a wide range of CO_2 concentrations. *Tellus A*, *72*(1), 1–19. https://doi.org/10.1080/16000870.2019.1699387

Dygert, B. D., & Hartmann, D. L. (2022). Sea surface temperature contrast in tropical world [Dataset]. (model data). Retrieved from http://hdl.handle.net/1773/46293

Emanuel, K., Wing, A. A., & Vincent, E. M. (2014). Radiative-convective instability. *Journal of Advances in Modeling Earth Systems*, *6*(1), 75–90. https://doi.org/10.1002/2013ms000270

Gasparini, B., Blossey, P. N., Hartmann, D. L., Lin, G. X., & Fan, J. W. (2019). What drives the life cycle of tropical anvil clouds? *Journal of Advances in Modeling Earth Systems*, *11*(8), 2586–2605. https://doi.org/10.1029/2019ms001736

Harrison, E. F., Minnis, P., Barkstrom, B. R., Ramanathan, V., Cess, R. D., & Gibson, G. G. (1990). Seasonal variation of cloud radiative forcing derived from the earth radiation budget experiment. *Journal of Geophysical Research*, *95*(D11), 18687–18703. https://doi.org/10.1029/jd095id11p18687

Hartmann, D. L., & Dygert, B. D. (2022). Global radiative convective equilibrium with a slab ocean: SST contrast, sensitivity and circulation. *Journal of Geophysical Research: Atmospheres*, *127*(12), e2021JD036400. https://doi.org/10.1029/2021JD036400

Hartmann, D. L., Dygert, B. D., Blossey, P. N., Fu, Q., & Sokol, A. B. (2022). The vertical profile of radiative cooling in radiative-convective equilibrium: Moist adiabat versus entrainment-modified plume model. *Journal of Climate.*, *35*(19), 2653–2665. https://doi.org/10.1175/JCLI-D-21-0861.1

Hartmann, D. L., Gasparini, B., Berry, S. E., & Blossey, P. N. (2018). The life cycle and net radiative effect of tropical anvil clouds. *Journal of Advances in Modeling Earth Systems*, *10*(12), 3012–3029. https://doi.org/10.1029/2018ms001484

Huang, J.-D., & Wu, C.-M. (2022). A framework to evaluate convective aggregation: Examples with different microphysics schemes. *Journal of Geophysical Research: Atmospheres*, *127*(5), e2021JD035886. https://doi.org/10.1029/2021JD035886

Neelin, J. D., & Held, I. M. (1987). Modeling tropical convergence based on the moist static energy budget. *Monthly Weather Review*, *115*(1), 3–12. https://doi.org/10.1175/1520-0493(1987)115⟨0003:Mtcbot⟩2.0.Co;2

Nuijens, L., & Emanuel, K. (2018). Congestus modes in circulating equilibria of the tropical atmosphere in a two-column model. *Quarterly Journal of the Royal Meteorological Society*, *144*(717), 2676–2692. https://doi.org/10.1002/qj.3385

Pierrehumbert, R. T. (1995). Thermostats, radiator fins, and the local runaway greenhouse. *Journal of the Atmospheric Sciences*, *52*(10), 1784–1806. https://doi.org/10.1175/1520-0469(1995)052⟨1784:TRFATL⟩2.0.CO;2

Popke, D., Stevens, B., & Voigt, A. (2013). Climate and climate change in a radiative-convective equilibrium version of ECHAM6. *Journal of Advances in Modeling Earth Systems*, *5*(1), 1–14. https://doi.org/10.1029/2012MS000191

Raymond, D. J., Sessions, S. L., Sobel, A. H., & Fuchs, Z. (2009). The mechanics of gross moist stability. *Journal of Advances in Modeling Earth Systems*, *1*(3). https://doi.org/10.3894/james.2009.1.9

Reed, K. A., Medeiros, B., Bacmeister, J. T., & Lauritzen, P. H. (2015). Global radiative-convective equilibrium in the community atmosphere model, version 5. *Journal of the Atmospheric Sciences*, *72*(5), 2183–2197. https://doi.org/10.1175/jas-d-14-0268.1

Tompkins, A. M., & Craig, G. C. (1998). Radiative-convective equilibrium in a three-dimensional cloud-ensemble model. *Quarterly Journal of the Royal Meteorological Society*, *124*(550), 2073–2097. https://doi.org/10.1002/qj.49712455013

Tompkins, A. M., & Semie, A. G. (2021). Impact of a mixed ocean layer and the diurnal cycle on convective aggregation. *Journal of Advances in Modeling Earth Systems*, *13*(12), e2020MS002186. https://doi.org/10.1029/2020MS002186

Wall, C. J., Hartmann, D. L., & Norris, J. R. (2019). Is the net cloud radiative effect constrained to be uniform over the tropical warm pools? *Geophysical Research Letters*, *46*(21), 12495–12503. https://doi.org/10.1029/2019gl083642

Wing, A. A., Emanuel, K., Holloway, C. E., & Muller, C. (2017). Convective self-aggregation in numerical simulations: A review. *Surveys in Geophysics*, *38*(6), 1173–1197. https://doi.org/10.1007/s10712-017-9408-4

Zhou, C., Zelinka, M. D., & Klein, S. A. (2016). Impact of decadal cloud variations on the Earth's energy budget. *Nature Geoscience*, *9*(12), 871–874. https://doi.org/10.1038/ngeo2828